Enhancing Interfacial Ferromagnetism and Magnetic Anisotropy of CaRuO$_3$/SrTiO$_3$ Superlattices via Substrate Orientation

Wenxiao Shi, Jie Zheng, Zhe Li, Mengqin Wang, Zhaozhao Zhu, Jine Zhang, Hui Zhang, Yunzhong Chen, Fengxia Hu, Baogen Shen, Yuansha Chen,* and Jirong Sun*

Artificial oxide heterostructures have provided promising platforms for the exploration of emergent quantum phases with extraordinary properties. One of the most interesting phenomena is the interfacial magnetism formed between two non-magnetic compounds. Here, a robust ferromagnetic phase emerged at the (111)-oriented heterointerface between paramagnetic CaRuO$_3$ and diamagnetic SrTiO$_3$ is reported. The Curie temperature is as high as $\approx$155 K and the saturation magnetization is as large as $\approx$1.3 μ_B per formula unit for the (111)-CaRuO$_3$/SrTiO$_3$ superlattices, which are obviously superior to those of the (001)-oriented counterparts and are comparable to the typical itinerant ferromagnet SrRuO$_3$. A strong in-plane magnetic anisotropy with six-fold symmetry is further revealed by the anisotropic magnetoresistance measurements, presenting a large in-plane anisotropic field of 3.0–3.6 T. More importantly, the magnetic easy axis of the (111)-oriented superlattices can be effectively tuned from $\langle 11\bar{2}1 \rangle$ to $\langle 1\bar{1}0 \rangle$ directions by increasing the layer thickness of SrTiO$_3$. The findings demonstrate a feasible approach to enhance the interface coupling effect by varying the stacking orientation of oxide heterostructures. The tunable magnetic anisotropy also shows potential applications in low-power-consumption or exchange spring devices.

1. Introduction

Perovskite transition-metal oxides with strongly correlated electrons have exhibited a rich variety of fascinating properties, such as charge-orbital ordering, high-temperature superconductivity, colossal magnetoresistance, and half-metallicity.[1–4] More

interestingly, artificial growth of the transition-metal oxide heterostructures (TMOHs) with atomic precision offers the prospect of greatly enhancing these exotic properties or realizing novel functionalities.[5–10] Among the TMOHs, heterostructures composed of magnetically active materials are especially fascinating, with the discoveries of interfacial ferromagnetic (FM) phases in the heterostructures of paramagnet/ferromagnet, paramagnet/antiferromagnet, or even paramagnet/diamagnet.[11–14] The interfacial FM phases with obviously low-dimensional features are highly relevant for technological applications, such as magnetic sensors, memories or read heads.[15] In particular, the enhanced interlayer coupling between charge, spin, orbital, and lattice degrees of freedom at oxide interface makes it an ideal platform for the manipulation of magnetic anisotropy (MA) of the emergent FM state, which plays a critical role in the design of fast-switching and low-power-consumption devices.

The 4d perovskite SrRuO$_3$ (SRO) has received intensive attention owing to the coexistence of itinerant ferromagnetism and strong spin-orbit coupling (SOC), which has great potential in spintronics/orbitronics applications as spin injector, spin-to-charge converter or spin-orbit torque unit.[16–19] However, due to weak electron-electron correlation, other 4d/5d perovskite oxides

W. Shi, J. Zheng, Z. Li, M. Wang, Z. Zhu, Y. Chen, F. Hu, B. Shen, Y. Chen, J. Sun
Beijing National Laboratory for Condensed Matter Physics and Institute of Physics
Chinese Academy of Sciences
Beijing 100190, China
E-mail: yschen@iphy.ac.cn; jrsun@iphy.ac.cn
W. Shi, J. Zheng, Z. Li, M. Wang, Z. Zhu, Y. Chen, F. Hu, B. Shen, Y. Chen, J. Sun
School of Physical Sciences
University of Chinese Academy of Sciences
Beijing 100049, China

The ORCID identification number(s) for the author(s) of this article can be found under https://doi.org/10.1002/smll.202308172

J. Zhang, H. Zhang
School of Integrated Circuit Science and Engineering
Beihang University
Beijing 100191, China
B. Shen
Ningbo Institute of Materials Technology and Engineering
Chinese Academy of Sciences
Ningbo, Zhejiang 315201, China
J. Sun
Spintronics Institute
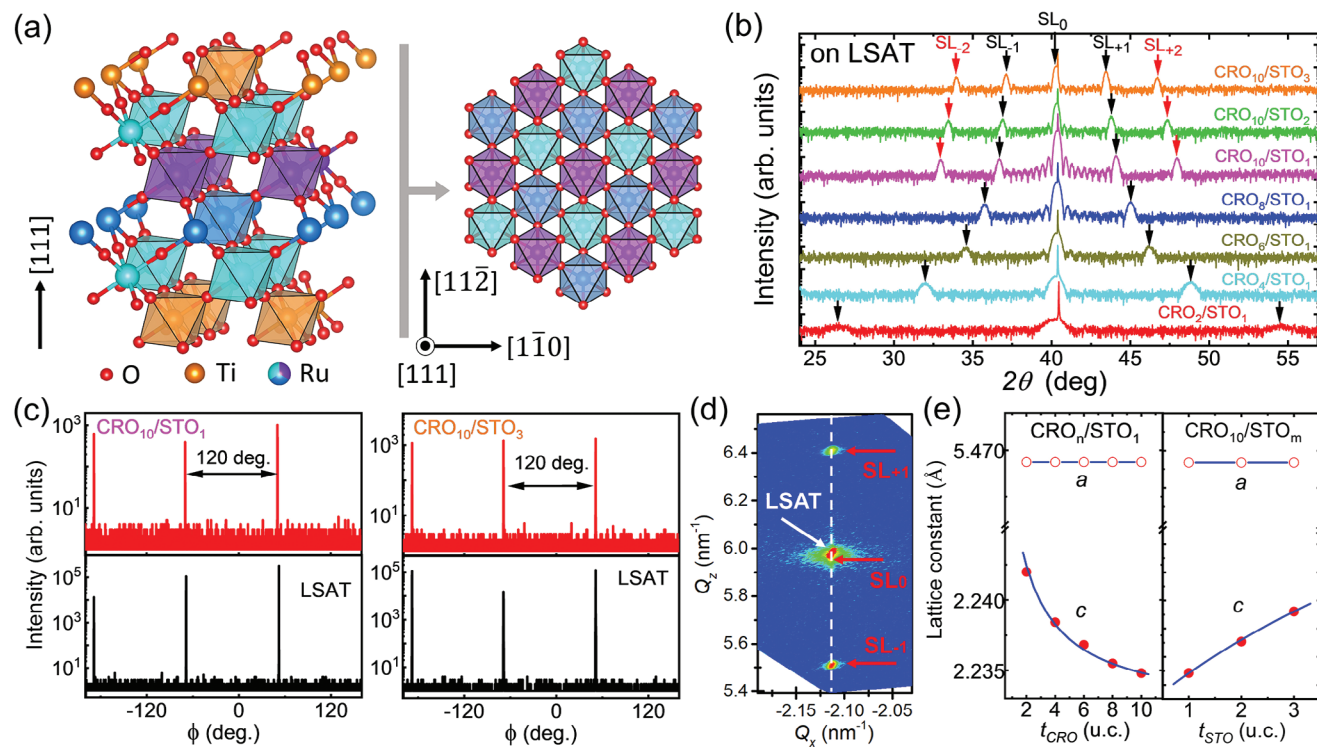University of Jinan
Jinan, Shandong 250022, China

Figure 1. a) Side view (left panel) and top view (right panel) of the atomic planes at the (111)-oriented CRO/STO interface. The Ca and Sr atoms are not pictured here. b) $\theta - 2\theta$ spectra for the $(CRO_n/STO_m)_{10}$ SLs on (111)-oriented LSAT substrate. SL_0 indicates (111) main peak and SL_{-1}, SL_{+1} indicate satellite peaks. c) ϕ-scans corresponding to (112) reflection of the $(CRO_{10}/STO_1)_{10}$ and $(CRO_{10}/STO_3)_{10}$ SLs. d) RSM $\approx$(112) reflection for the $(CRO_{10}/STO_3)_{10}$ SL. e) Lattice constants as functions of t_{CRO} or t_{STO}. Blue line is the ideal c-axis constants calculated by $c = (n \times c_{CRO} + m \times c_{STO})/(n + m)$, where c_{STO} and c_{CRO} represent the lattice constants of the STO and CRO sublayers, respectively.

do not host the FM order. As a sister material of SRO, CaRuO₃ (CRO) has the same GdFeO₃-typed orthorhombic structure with *Pbnm* symmetry and the same electron configuration of t_{2g}^4 for the Ru⁴⁺ ions.[20,21] The difference is, as the ionic radius of Ca²⁺ (1.08 Å) is much smaller than Sr²⁺ (1.31 Å), the orthorhombic distortion of RuO₆ octahedra in CRO has approximately doubled than that in SRO, bending the Ru—O—Ru bond angle to 150° as compared to 163° in SRO.[22–24] Thus, CRO maintains a paramagnetic (PM) metal in either bulk or thin film form.[24–31] Introducing magnetic order into CRO is an attractive topic for either experimental or theoretical research.[27–31] Weak FM order has been reported in CRO films by different chemical doping, including Ti doping, H⁺ intercalation and δ-doping via introducing a SrO monolayer.[28–31] However, the resulting FM state was not robust, showing the Curie temperature (T_C) and saturation magnetization (M_S) much lower than those shown by SRO. Recently, we reported FM order in the (001)-oriented CRO layer sandwiched by SrTiO₃ (STO) layers, and ascribed this phenomenon to a reduced tilting/rotation of the RuO₆ octahedra at CRO/STO interface.[14] The highest T_C is ≈120 K and M_S is ≈0.7 μ_B per formula unit (f.u.), which are obviously superior to previously reported values, indicating the specificity of the CRO/STO interlayer coupling.

While the former work was carried out on the CRO/STO stacking along the [001] crystallographic direction,[14] here we turn our attention to the (111)-oriented counterpart. A schematic of the interface configuration is depicted in **Figure 1**a (left panel for

side view and right panel for top view). By growing superlattices along the [111] direction, each interfacial Ru cation has three Ru neighbors and three Ti neighbors. As a result, the interlayer interaction between Ru and Ti ions will be enhanced compared to the conventional (001)-stacking. Moreover, the B site ions form the trigonal symmetric lattice structure in the (111) plane. The trigonal crystal-field symmetry together with a sizable SOC in (111)-oriented thin films may result in a topologically nontrivial band structure.[32–34] For example, Chandra et al. predicted that emergent FM phases with the T_C up to room temperature could be achieved in the (111) superlattices (SLs) due to quantum confinement.[35] Therefore, the (111)-oriented TMOHs are promising platforms for realizing various topological phases.

Here, we report the FM phase induced in the interface layers of (111)-oriented CRO/STO SLs. Via the investigation of anomalous hall effect, magnetoresistance and magnetic properties, we demonstrate that the interfacial FM phase is much more robust in the (111)-SLs than in the (001)-SLs. The highest T_C is ≈155 K and the largest M_S is ≈1.3 μ_B f.u⁻¹. for the (111)-oriented SLs, comparable to the corresponding values of bulk SRO phase. A strong in-plane magnetic anisotropy (MA) with sixfold symmetry is further revealed by anisotropic magnetoresistance (AMR) measurements. More importantly, the magnetic easy axis in the (111) plane can be tuned by varying the layer thickness of STO, varying from the ⟨11$\bar{2}$⟩ direction to ⟨1$\bar{1}$0⟩ direction when the layer thickness of STO increases from 1 to 3 unit cells (u.c.). Our findings demonstrate a feasible way to manipulate interface coupling and
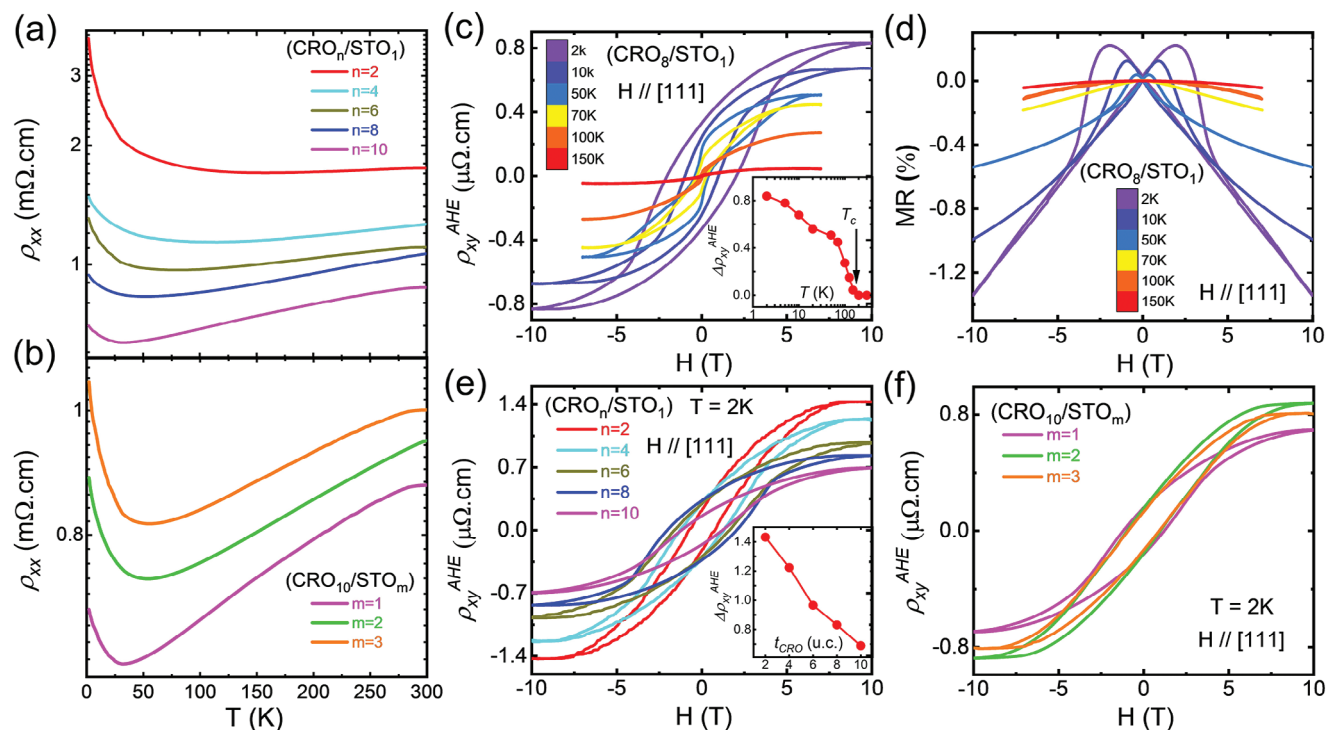
**ADVANCED
SCIENCE NEWS**

www.advancedsciencenews.com

NANO · MICRO

small

www.small-journal.com

Figure 2. a) ρ_{xx}-T curves for $(CRO_n/STO_1)_{10}$ and b) $(CRO_{10}/STO_m)_{10}$ SLs on (111)-oriented LSAT substrate. c) ρ_{xy}^{AHE}-H and d) MR–H curves of $(CRO_8/STO_1)_{10}$ SL measured from 2 K to 150 K. e) ρ_{xy}^{AHE}-H curves at 2 K for $(CRO_n/STO_1)_{10}$ and f) $(CRO_{10}/STO_m)_{10}$ SLs.

thus exotic interfacial phases by the stacking directions of oxide heterostructures.

2. Results and Discussion

2.1. Structural Analysis

Epitaxial $(CRO_n/STO_m)_{10}$ SLs, consisting of n u.c. of CRO and m u.c. of STO, were grown on (111)-oriented $(LaAlO_3)_{0.3}(SrAl_{0.5}Ta_{0.5}O_3)_{0.7}$ (LSAT) substrate by pulsed laser deposition. Details on the growth process are provided in the Methods section. Here, one unit cell (111)-oriented layer has a thickness equal to the distance between two nearest (111) planes (d_{111}). To reveal the effect of sublayer thickness on interlayer coupling, two series of SLs, $(CRO_n/STO_1)_{10}$ (n = 2, 4, 6, 8, 10) and $(CRO_{10}/STO_m)_{10}$ (m = 1, 2, 3), were prepared. The epitaxial growth of the (111)-SLs is verified by the X-ray diffraction of θ −2θ scan and ϕ-scan. The θ −2θ spectra are presented in Figure 1b for all SLs investigated. Clear (111) Bragg peaks with thickness fringes are observed, indicating the good crystallinity and smooth surface of the samples. Distinct satellite peaks are further detected, confirming the formation of SL structure. The satellite peaks shift toward the (111) main peak as n and m increases, which is a general feature of the XRD spectra of SLs. The ϕ-scans of the (112) reflection are shown in Figure 1c: The left and right panels correspond to samples of $(CRO_{10}/STO_1)_{10}$ and $(CRO_{10}/STO_3)_{10}$ SLs, respectively. Obviously, the ϕ-scan spectra of the substrate and the SL show the in-phase threefold symmetry, supporting the (111) epitaxial growth of the SLs with a honeycomb lattice. To further determine the in-plane strain

state of the SLs, the reciprocal space mapping (RSM) of the (112) reflection is measured. Taking $(CRO_{10}/STO_3)_{10}$ as an example, the diffraction spots of the SL (marked by red arrow) are vertically aligned with the diffraction spot of substrate (Figure 1d), i.e., the SL is coherently strained to the substrate without lattice relaxations. This conclusion is also applicable to other samples (see Figure S2, Supporting Information). Based on the results of RSM and θ −2θ scanning, the a- and c-axis lattice constants of the SLs have been deduced. As shown in Figure 1e, the c-axis lattice constant displays a smooth decrease with the increase of the CRO layer thickness. This is understandable noting the fact that CRO has a smaller lattice constant as compared to STO (3.85 Å vs 3.91 Å). As reported, the bulk phase of CRO is orthorhombic, with the lattice constants of a_o = 5.36, b_o = 5.54, and c_o = 7.68 Å.[20,21] Alternatively, it can be described by a pseudo-cubic phase with a lattice parameter of 3.85 Å. Similarly, fixing the thickness of CRO layer, the c-axis lattice constant gradually increases with the increase of the STO layer thickness.

2.2. Transport Behaviors with Magnetic Features

To explore the effect of interface engineering, the transport properties of the SLs are investigated. **Figure 2**a,b shows the longitudinal resistivity (ρ_{xx}) as a function of temperature (T) for the $(CRO_n/STO_1)_{10}$ and $(CRO_{10}/STO_m)_{10}$ SLs, respectively. As expected, the SLs with thick CRO sublayers are basically metallic, with a slight resistance upturn emerging at low temperatures. Noting that the CRO bare film is well metallic and STO is strongly insulating, the transport behavior of SLs is dominated by the

**ADVANCED
SCIENCE NEWS**

www.advancedsciencenews.com

**NANO · MICRO
small**

www.small-journal.com

CRO sublayers. For the $(CRO_n/STO_1)_{10}$ SLs, the ρ_{xx} gradually increases with the decrease of the CRO layer thickness (t_{CRO}). This can be ascribed to enhanced interface scattering in the samples with ultrathin CRO sublayers. The ρ_{xx}–T dependence shows very similar trend for the $(CRO_{10}/STO_m)_{10}$ samples, and ρ_{xx} increases with the increase of STO layer thickness (t_{STO}). This indicates that the STO layer is much more resistive than the CRO layer.

Further Hall measurements reveal the distinct properties of the CRO sublayers. As a function of magnetic field (H), Figure 2c shows the anomalous Hall resistivity (ρ_{xy}^{AHE}) for a typical sample $(CRO_8/STO_1)_{10}$ collected at different temperatures. Remarkably, clear ρ_{xy}^{AHE}–H hysteresis loops are observed at temperature below 100 K. Although the magnetic hysteresis disappears at temperature above ≈100 K, AHE remains visible up to 150 K. As mentioned above, the transport properties of the $(CRO_n/STO_1)_{10}$ SLs are determined by CRO sublayers. The AHE curves unambiguously suggest the establishment of long-range FM order in CRO. This is similar to the results observed in the (001)-oriented CRO/STO SLs,[14] indicating the inducing of the FM state in CRO by neighboring STO is independent of film orientation. To get further information on the emergent ferromagnetism, the saturation value of the anomalous Hall resistivity ($\Delta\rho_{xy}^{AHE}$) is deduced from the ρ_{xy}^{AHE}–H relation and plotted as a function of T in the inset of Figure 2c. With the increase of temperature, the $\Delta\rho_{xy}^{AHE}$ experiences a monotonic decrease, varying from ≈0.85 μΩ cm at 2 K to ≈0.04 μΩ cm at 150 K. Extrapolating the $\Delta\rho_{xy}^{AHE}$–T relation to the limit of $\Delta\rho_{xy}^{AHE} = 0$, we obtained the Curie temperature T_C of ≈155 K. This transition temperature is significantly higher than the T_C obtained in the (001)-oriented CRO/STO SLs, where the highest T_C is 120 K. More importantly, it is comparable to the typical itinerant ferrimagnet SRO with a T_C of ≈150 K in thin film forms.[36–38] In addition to $\Delta\rho_{xy}^{AHE}$, the coercivity field (H_C), as a prominent feature of magnetic materials, maintains a higher temperature for the (111) SLs compared to that of the (001) SLs. As shown, the H_C is as large as ≈2 T at 2 K and remains sizable up to 100 K. In contrast, for the (001) SLs, the hysteresis behavior of ρ_{xy}^{AHE}–H curves can be only identified at temperatures below 20 K.[14] All these features suggest that the induced interfacial FM state seems to be more robust in the (111) case than in the (001) case. The magnetoresistance (MR) measurements also support the formation of the FM order in the SLs. Figure 2d depicts the magnetic field dependence of MR = $(R_H\text{-}R_0)/R_0$ obtained at different temperatures for $(CRO_8/STO_1)_{10}$ SL, where R_0 and R_H are the longitudinal resistances measured without and with an out-of-plane field, respectively. Butterfly-shaped MR–H loops with two broad peaks corresponding to $\pm H_C$ are clearly seen, which indicates the reconstruction of magnetic domains in the CRO layer under the applied magnetic field. Same as the $\Delta\rho_{xy}^{AHE}$, the MR value recorded at 10 T decreases sharply during the warming process, varying from −1.34% at 2 K to −0.04% at 150 K.

It is worth pointing out that the emergence of ferromagnetism is a generic property of all samples studied here. Figure 2e,f presents the ρ_{xy}^{AHE}–H loops obtained at 2 K for the $(CRO_n/STO_1)_{10}$ ($n = 2, 4, 6, 8, 10$) and $(CRO_{10}/STO_m)_{10}$ ($m = 1, 2, 3$) SLs, respectively. The highest $\Delta\rho_{xy}^{AHE}$ appears in the $(CRO_2/STO_1)_{10}$ SL, a sample with the thinnest CRO sublayer. With the in-

crease of CRO layer thickness, $\Delta\rho_{xy}^{AHE}$ exhibits a monotonic decrease, from ≈1.43 μΩ cm for $t_{CRO} = 2$ u.c. to ≈0.7 μΩ cm for $t_{CRO} = 10$ u.c.. This is a fingerprint of interfacial effect that is the FM order established in the near interface region of CRO. For the $(CRO_{10}/STO_m)_{10}$ SLs (Figure 2f), in contrast, the $\Delta\rho_{xy}^{AHE}$ and H_C change slightly with the increased thickness of the STO layer. All these features suggest that the induced-FM state exists only in the near interface region of the CRO layers in the SLs.

2.3. SQUID Magnetic Characterizations

The transport measurements reveal the establishment of FM order in the CRO sublayers. To get direct information on the FM state, the magnetic properties of the SLs are further investigated. **Figure 3**a shows the temperature (T) dependence of the magnetization (M) for the two sets of SLs, obtained with an out-of-plane field of 0.05 T in field-cooling mode. The magnetic result of a bare CRO film, which is PM, is also presented for comparison. Unlike that of the PM CRO bare film, the magnetization of the SL displays a rapid increase when cooled below T_C and a smooth tendency toward saturation when temperature is low enough, signifying the PM–FM transition. Figure 3b shows the magnetic field dependence of magnetization (M–H), recorded at 5 K. Similar to the anomalous Hall loops, magnetic hysteresis is clearly observed for all SLs. The dependence of T_C and M_S on t_{CRO} is summarized in Figure 3c,d for the (111)-oriented SLs. Here, the T_C is defined by the zero-crossing temperature of the tangent line (see Figure S3, Supporting Information). The results obtained in the (001)-oriented SLs are also given for comparison.[14] The T_C of the (111)-oriented SLs displays a strong dependence on t_{CRO}, first increasing and then decreasing as t_{CRO} grows from 2 u.c. to 10 u.c.. This non-monotonic dependence of T_C on t_{CRO} is similar to that for the (001) samples, which is a consequence of the competition between increased dimensionality and decreased exchange energy as t_{CRO} grows. In principle, the T_C of the CRO layer is jointly determined by the exchange interaction between Ru ions and the coordination number of the Ru ion. Since the Ru ion at CRO/STO interface has a relatively low coordination number, the T_C of the ultrathin CRO layer is low. The effective coordination number will increase as the layer thickness of CRO grows, favoring a high T_C. However, when the CRO layer is thick enough, the exchange interaction between Ru ions will be weakened since the ferromagnetism is an interfacial effect, appearing only in the near interface region. As a consequence, T_C undergoes an increase-to-decrease crossover as t_{CRO} grows. More importantly, we find that the maximal T_C of the $(CRO_8/STO_1)_{10}$ SL (≈155 K) is ≈35 K higher than that of the (001)-oriented SLs, as high as that of the SRO thin films (150 K). Unlike T_C, the M_S of the (111)-oriented SLs displays a monotonic decrease with increased t_{CRO}, varying from ≈1.3 μB f.u⁻¹. for $t_{CRO} = 2$ u.c. to ≈0.36 μB f.u⁻¹. for $t_{CRO} = 10$ u.c.. As shown in Figure 3d, from (001) to (111) orientation, the maximal M_S is nearly doubled. Such an enhancement in M_S reminds us of the results of SRO bare films, for which a higher saturation moment was obtained in the (111)-oriented film as compared to the (001)-oriented film (see Figure S4, Supporting Information). Compared to the drastic changes of M_S with the thickness of CRO layer, the
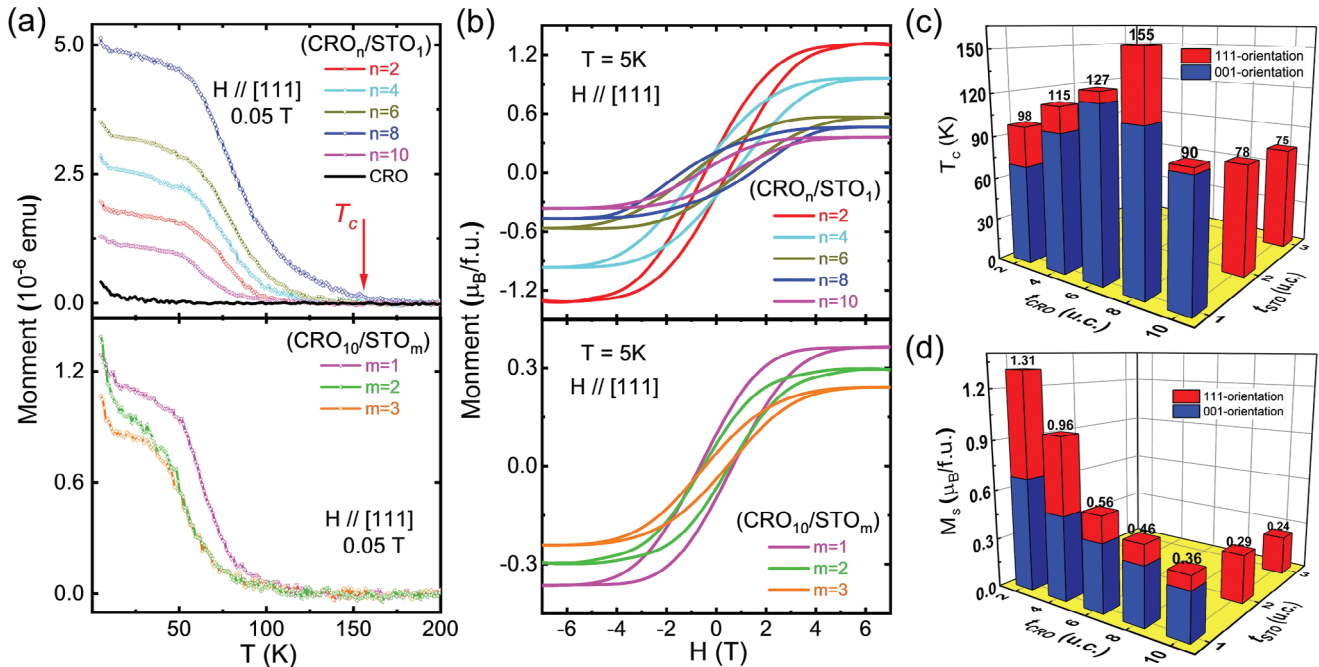
**ADVANCED
SCIENCE NEWS**

www.advancedsciencenews.com

NANO · MICRO

small

www.small-journal.com

Figure 3. a) $M–T$ curves for $(CRO_n/STO_1)_{10}$ and $(CRO_{10}/STO_m)_{10}$ SLs on (111)-oriented LSAT substrate, measured with an out-of-plane field of 0.05 T in field-cooling mode. b) $M–H$ curves for $(CRO_n/STO_1)_{10}$ and $(CRO_{10}/STO_m)_{10}$ SLs on (111)-oriented LSAT substrate, showing clear magnetic hysteresis loops. c) T_C and d) M_S as functions of t_{CRO} and t_{STO}, respectively, for the SLs on LSAT.

thickness of STO layer has limited influence on the magnetic properties. With a constant CRO layer thickness of 10 u.c., the M_S reduces from $\approx 0.36\,\mu_B$ f.u.$^{-1}$. for $t_{STO} = 1$ u.c. to $\approx 0.24\,\mu_B$ f.u.$^{-1}$. for $t_{STO} = 3$ u.c.. This slight degeneration may be due to the weakening of magnetic coupling between the FM CRO layers separated by the thicker nonmagnetic STO layers.

2.4. Magnetic Anisotropy of $(CROn/STOm)_{10}$ Superlattices

Above results reveal a more robust FM state formed at the (111)-CRO/STO interface than that formed at the (001)-CRO/STO interface. Another interesting question is the change in MA with the substrate orientation. To reveal the MA of the CRO/STO SLs, we first compare the $MR–H$ curves measured with magnetic field applied along three typical crystal orientations of the (111) films that is the in-plane $[1\bar{1}0]$, $[11\bar{2}]$ and the out-of-plane [111] directions. As shown in **Figure 4**a,b, similar butterfly-shaped hysteresis loops are observed in all MR curves (see Figure S5, Supporting Information), but the magnitude of MR is obviously different. Generally, for a ferromagnet, the negative MR under external magnetic field is due to the reduced spin-flip scattering, which will be more remarkable when magnetic field (H) applied along the easy-axis direction.[39,40] We can see that the amplitude of MR with H along the in-plane directions ($[11\bar{2}]$ or $[1\bar{1}0]$) is always larger than that obtained in the [111] direction, indicating the magnetic axis lies in-plane. An interesting observation is that the MR amplitude in the $[11\bar{2}]$ direction is larger than that in the $[1\bar{1}0]$ direction for the $(CRO_n/STO_1)_{10}$ SLs, while this order is reversed in the $(CRO_{10}/STO_3)_{10}$ SL. This possibly suggests that the magnetic easy-axis of CRO layers has rotated by

90° when the layer thickness of STO increases. To clearly reveal the MA symmetry, we conducted the measurements of angular dependent anisotropic magnetoresistance (AMR) with in-plane fields. Figure 4c–f present the AMR-θ curves for four typical SLs measured at $H = 10$ T and $T = 2$ K. Here, AMR is defined as $AMR = (R_\theta - R_0)/R_0$, where R_θ is the resistance measured with an in-plane field that forms an angle of θ with the current applied along $[1\bar{1}0]$ (see the inset of Figure 4a). From first glance, the AMR contains two oscillations: One is sixfold-symmetric (red dashed lines) and another is twofold-symmetric (blue dashed lines). This phenomenon is observed in all SLs though detailed features vary from sample to sample as shown in Figure S6 (Supporting Information). We can see that the sixfold-symmetric oscillations for the $(CRO_n/STO_1)_{10}$ SLs all show six valleys at $\theta = 30° + i \times 60°$($i = 0 - 5$) (i.e., the $\langle 11\bar{2} \rangle$ directions), the amplitude of which reduces from 2% for n = 2 to 0.5% for n = 10. For the $(CRO_{10}/STO_3)_{10}$ SL, however, the six valleys have shifted to the positions of $\theta = i \times 60°$($i = 0 - 5$) (i.e., the $\langle 1\bar{1}0 \rangle$ directions), being consistent with the MR curves in Figure 4b. Different from the sixfold-symmetric term, the twofold-symmetric oscillations always show two valleys at $\theta = 0°$, 180° and two peaks at $\theta = 90°$, 270°, with nearly a constant amplitude independent of the thickness of either CRO or STO layers. To get an idea for the origin of the two AMR oscillations, we further measured the AMR curves at 2, 10, 50 and 150 K (a temperature well above T_C). Figure 4g–i are the temperature dependence of the AMR polar plots for the $(CRO_2/STO_1)_{10}$, $(CRO_{10}/STO_1)_{10}$, and $(CRO_{10}/STO_3)_{10}$ SLs, respectively. As shown, the mixed sixfold/twofold oscillations are observed at low temperatures, and only the twofold oscillation remains when $T > T_C$. This is a strong indication that the sixfold AMR oscillation is originated
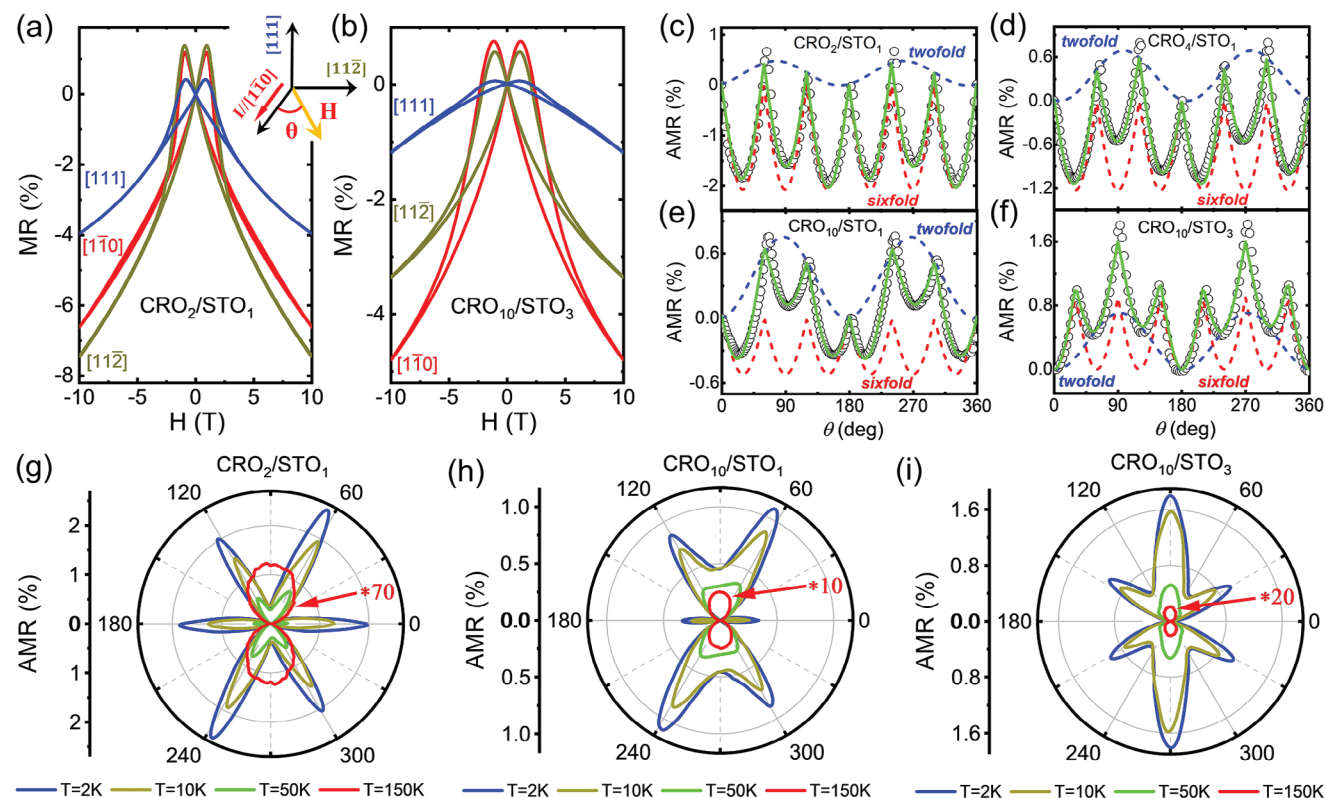
Figure 4. a) The MR at T = 2 K for $(CRO_2/STO_1)_{10}$ and b) $(CRO_{10}/STO_3)_{10}$ SLs with the magnetic field applied parallel to $[1\bar{1}0]$, $[11\bar{2}]$ and $[111]$ directions. c) Angle dependent AMR for $(CRO_2/STO_1)_{10}$, d) $(CRO_4/STO_1)_{10}$, e) $(CRO_{10}/STO_1)_{10}$ and f) $(CRO_{10}/STO_3)_{10}$ SLs. Black symbols are experimental data. Green lines are the results of curve fitting. Red and blue lines are sixfold and twofold components, respectively. g) Polar plots of in-plane AMR of the $(CRO_2/STO_1)_{10}$, h) $(CRO_{10}/STO_1)_{10}$ and i) $(CRO_{10}/STO_3)_{10}$ SLs measured under a magnetic field of 10 T and at different temperatures ranging from 2 K to 150 K. The geometry of the AMR measurement is shown in the inset of Figure 4a. The electric current is applied along the $[1\bar{1}0]$ direction and the magnetic field is rotated in the (111) plane, forming an angle of θ with applied current.

from magnetic contribution while the twofold AMR oscillation is originated from non-magnetic contributions, such as Lorentz scattering or normal AMR.[41,42] Thus, it is natural that the $(CRO_2/STO_1)_{10}$ SL with the highest M_S presents the maximal sixfold AMR amplitude. More importantly, the switching of the valley position from $\theta = 30°$ to $\theta = 0°$ clearly confirms that the rotation of magnetic easy axis from the $\langle 11\bar{2} \rangle$ to the $\langle 1\bar{1}0 \rangle$ direction while increasing the layer thickness of STO from 1 to 3 u.c..

It should be further pointed out that the AMR of (111)-oriented SLs show a broad curvature around the magnetic easy-axis and a sharp tip around the magnetic hard-axis. This is different from that observed for the (001)-oriented SLs, in which the AMR follows the general cosine square angular-dependence.[14] This usually implies a strong magnetization pinning effect close to the easy-axis for the (111) SLs, which is also observed for the $La_{1-x}Sr_xMnO_3$, Co(fcc), $Fe_{30}Co_{70}$ films in previous works.[43–45] The deviation from cosine square angular-dependence comes from the fact that the magnetization M cannot be coherently saturated in the direction of applied field H when H is rotated to the angles far away from the easy axis. By considering this effect, we find the experimental data can be well reproduces by the formula:

$$AMR = c_2 \times \cos(2\theta - \omega_2) + c_6 \times \cos[6 \times (\theta - \alpha(\theta)) - \omega_6] \quad (1)$$

$$\alpha(\theta) = \frac{\sin(6\theta)}{4H/H_a^{in} + 6 \times \cos(6\theta)} \quad (2)$$

where c_2 and c_6 are the amplitudes of twofold and sixfold oscillations, ω_2 and ω_6 are the corresponding offset angles. $\alpha(\theta)$ describes the angle between M and H, where H_a^{in} is the in-plane anisotropic filed (Details of formula derivation are provided in Section S1, supporting information). Satisfactory agreement with experiment results is obtained by adopting suitable fitting parameters. The deduced in-plane anisotropic field for the SLs is ≈3.0–3.6 T. All these features indicate that (111)-oriented CRO/STO SLs have a strong in-plane MA. Thus, the effective tuning of magnetic easy axis by the thickness of STO insert layer has far-reaching scientific and technological implications, such as the low-power-consumption or exchange spring applications.

3. Conclusion

To summarize, we demonstrate a robust interfacial FM state in the (111)-oriented CRO/STO SLs, showing the highest T_C of ≈155 K and largest M_S of ≈1.3 μ_B f.u^{-1}. that are both significantly better than those of the (001)-oriented SLs. In addition, a nontrivial in-plane MA is revealed in the (111)-oriented SLs, which can be

effectively tuned from the $\langle 11\bar{2} \rangle$ to $\langle 1\bar{1}0 \rangle$ directions by precisely controlling the thickness of STO insert layer. Our findings provide an approach for enhancing the interface coupling and thus induced emergent phases in oxide heterostructures. The tunable magnetic easy axis with the non-magnetic insert layer may give some hints to other systems with (111) crystal orientation.

4. Experimental Section

Sample Fabrication: High quality $(CRO_n/STO_m)_{10}$ SLs were epitaxially grown on (111)-oriented LSAT substrates by the technique of pulsed laser deposition (KrF, $\lambda = 248$ nm). A bare CRO film with thickness of 50 u.c. was also prepared for comparison. Prior to sample deposition, the (111)-oriented LSAT substrate was annealed in oxygen pressure of 1 atm at 900 °C for 2 h. During film growth, the substrate temperature was kept at 670 °C and the oxygen pressure was set to 40 Pa. The adopted fluence of laser pulse was 1.2 J cm^{-2} and the repetition rate was 2 Hz. After deposition, a post-annealing in an oxygen pressure of $\approx$200 Pa was performed to reduce the oxygen vacancies in the CRO or the STO sublayers. The deposition rate for the CRO and STO layers had been carefully calibrated by the technique of small angle X-ray reflectivity (XRR, see Figure S1, Supporting Information).

Sample Characterization: The surface morphology of as-prepared films was measured by atomic force microscopy (AFM, SPI 3800N, Seiko). The crystal structure was determined by a high-resolution X-ray diffractometer (D8 Discover, Bruker) with the Cu-Kα radiation. The magnetic properties were measured by a Quantum Designed vibrating sample magnetometer (VSM-SQUID) in the temperature range of 5–300 K, with a maximal magnetic field of 7 T. The magnetic field was applied along the out-of-plane direction of the (111) films. The transport measurements were performed in Quantum Designed physical property measurement system (PPMS) with standard Hall bar geometry. For the transport measurements, the SL samples were further patterned to a Hall bar-shaped device by the conventional lithography and Ar-ions etching technique, with a width of 200 µm and a length of 1300 µm. The optical image of a typical Hall bar device is given in Figure S1d (Supporting Information). All electric measurements were performed in the DC mode, with an applied current of 1 µA.

Supporting Information

Supporting Information is available from the Wiley Online Library or from the author.

Acknowledgements

Conflict of Interest

The authors declare no conflict of interest.

Data Availability Statement

The data that support the findings of this study are available from the corresponding author upon reasonable request.

Keywords

[1] H. Takagi, H. Y. Hwang, *Science* **2010**, *327*, 1601.
[2] M. Imada, A. Fujimori, Y. Tokura, *Rev. Mod. Phys.* **1998**, *70*, 1039.
[3] E. Dagotto, *Science* **2005**, *309*, 257.
[4] Y. Tokura, N. Nagaosa, *Science* **2000**, *288*, 462.
[5] S. Okamoto, A. J. Millis, *Nature* **2004**, *428*, 630.
[6] P. Yu, J.-S. Lee, S. Okamoto, M. D. Rossell, M. Huijben, C.-H. Yang, Q. He, J. X. Zhang, S. Y. Yang, M. J. Lee, Q. M. Ramasse, R. Erni, Y.-H. Chu, D. A. Arena, C.-C. Kao, L. W. Martin, R. Ramesh, *Phys. Rev. Lett.* **2010**, *105*, 027201.
[7] J. Matsuno, K. Ihara, S. Yamamura, H. Wadati, K. Ishii, V. V. Shankar, H.-Y. Kee, H. Takagi, *Phys. Rev. Lett.* **2015**, *114*, 247209.
[8] J. Matsuno, N. Ogawa, K. Yasuda, F. Kagawa, W. Koshibae, N. Nagaosa, Y. Tokura, M. Kawasaki, *Sci. Adv.* **2016**, *2*, 1600304.
[9] X. Liu, W. Song, M. Wu, Y. Yang, Y. Yang, P. Lu, Y. Tian, Y. Sun, J. Lu, J. Wang, Y. Dan, Y. Shi, N. X. Sun, Y. Sun, P. Gao, K. Shen, G. Chai, S. Kou, C.-W. Nan, J. Zhang, *Nat. Commun.* **2021**, *12*, 5453.
[10] S. W. Zeng, X. M. Yin, C. J. Li, L. E. Chow, C. S. Tang, K. Han, Z. Huang, Y. Cao, D. Y. Wan, Z. T. Zhang, Z. S. Lim, C. Z. Diao, P. Yang, A. T. S. Wee, S. J. Pennycook, A. Ariando, *Nat. Commun.* **2022**, *13*, 743.
[11] M. Gibert, P. Zubko, R. Scherwitzl, J. Iguez, J.-M. Triscone, *Nat. Mater.* **2012**, *11*, 195.
[12] J. D. Hoffman, B. J. Kirby, J. Kwon, G. Fabbris, D. Meyers, J. W. Freeland, I. Martin, O. G. Heinonen, P. Steadman, H. Zhou, C. M. Schlepütz, M. P. M. Dean, S. G. E. teVelthuis, J.-M. Zuo, A. Bhattacharya, *Phys. Rev. X* **2016**, *6*, 041038.
[13] J. Nichols, X. Gao, S. Lee, T. L. Meyer, J. W. Freeland, V. Lauter, D. Yi, J. Liu, D. Haskel, J. R. Petrie, E.-J. Guo, A. Herklotz, D. Lee, T. Z. Ward, G. Eres, M. R. Fitzsimmons, H. N. Lee, *Nat. Commun.* **2016**, *7*, 12721.
[14] W. Shi, J. Zhang, X. Chen, Q. Zhang, X. Zhan, Z. Li, J. Zheng, M. Wang, F. Han, H. Zhang, L. Gu, T. Zhu, B. Liu, Y. Chen, F. Hu, B. Shen, Y. Chen, J. Sun, *Adv. Funct. Mater.* **2023**, *33*, 2300338.
[15] M. Bibes, J. E. Villegas, A. Barthélémy, *Adv. Phys.* **2011**, *60*, 5.
[16] S. Emori, U. S. Alaan, M. T. Gray, V. Sluka, Y. Chen, A. D. Kent, Y. Suzuki, *Phys. Rev. B* **2016**, *94*, 224423.
[17] L. Wang, Q. Feng, H. G. Lee, E. K. Ko, Q. Lu, T. W. Noh, *Nano Lett.* **2020**, *20*, 2468.
[18] J. Wei, H. Zhong, J. Liu, X. Wang, F. Meng, H. Xu, Y. Liu, X. Luo, Q. Zhang, Y. Guang, J. Feng, J. Zhang, L. Yang, C. Ge, L. Gu, K. Jin, G. Yu, X. Han, *Adv. Funct. Mater.* **2021**, *31*, 2100380.
[19] R. J. Cava, *Dalton Trans* **2004**, *19*, 2979.
[20] R. J. Kennedy, R. Madden, P. A. Stampe, *J. Phys. D* **2001**, *34*, 1853.
[21] D. L. Proffit, H. W. Jang, S. Lee, C. T. Nelson, X. Q. Pan, M. S. Rzchowski, C. B. Eom, *Appl. Phys. Lett.* **2008**, *93*, 111912.
[22] P. Siwakoti, Z. Wang, M. Saghayezhian, D. Howe, Z. Ali, Y. Zhu, J. Zhang, *Phys. Rev. Mater.* **2021**, *5*, 114409.
[23] W. Bensch, *Solid State Ionics* **1990**, *43*, 171.

**ADVANCED
SCIENCE NEWS**

www.advancedsciencenews.com

NANO · MICRO

small

www.small-journal.com

[24] H. T. Dang, J. Mravlje, A. Georges, A. J. Millis, *Phys. Rev. B* **2015**, *91*, 195149.

[25] G. Cao, S. Mccall, M. Shepard, J. E. Crow, R. P. Guertin, *Phys. Rev. B* **1997**, *56*, 321.

[26] M. Schneider, V. Moshnyaga, P. Gegenwart, *Phys. Status Solidi B* **2010**, *247*, 577.

[27] A. T. Zayak, X. Huang, J. B. Neaton, K. M. Rabe, *Phys. Rev. B* **2008**, *77*, 214410.

[28] Z. Ali, M. Saghayezhian, Z. Wang, A. O'hara, D. Shin, W. Ge, Y. T. Chan, Y. Zhu, W. Wu, S. T. Pantelides, J. Zhang, *npj Quantum Mater.* **2022**, *7*, 108.

[29] S. C. Shen, Z. L. Li, Z. J. Tian, W. D. Luo, S. Okamoto, P. Yu, *Phys. Rev. X* **2021**, *11*, 021018.

[30] T. He, R. J. Cava, *Phys. Rev. B* **2001**, *63*, 172403.

[31] V. Hardy, B. Raveau, R. Retoux, N. Barrier, A. Maignan, *Phys. Rev. B* **2006**, *73*, 094418.

[32] R. Yu, W. Zhang, H.-J. Zhang, S.-C. Zhang, X. Dai, Z. Fang, *Science* **2010**, *329*,61.

[33] Z. Qiao, S. A. Yang, W. Feng, W.-K. Tse, J. Ding, Y. Yao, J. Wang, Q. Niu, *Phys. Rev. B* **2010**, *82*, 161414(R).

[34] T.-W. Chen, Z.-R. Xiao, D.-W. Chiou, G.-Y. Guo, *Phys. Rev. B* **2011**, *84*, 165453.

[35] H. K. Chandra, G.-Y. Guo, *Phys. Rev. B* **2017**, *95*, 134448.

[36] S. Thomas, B. Kuiper, J. Hu, J. Smit, Z. Liao, Z. Zhong, G. Rijnders, A. Vailionis, R. Wu, G. Koster, J. Xia, *Phys. Rev. Lett.* **2017**, *119*, 177203.

[37] H. G. Lee, L. Wang, L. Si, X. He, D. G. Porter, J. R. Kim, E. K. Ko, J. Kim, S. M. Park, B. Kim, A. T. S. Wee, A. Bombardi, Z. Zhong, T. W. Noh, *Adv. Mater.* **2020**, *32*, 1905815.

[38] W. Lin, L. Liu, Q. Liu, L. Li, X. Shu, C. Li, Q. Xie, P. Jiang, X. Zheng, R. Guo, Z. Lim, S. Zeng, G. Zhou, H. Wang, J. Zhou, P. Yang, Ariando, S. J. Pennycook, X. Xu, Z. Zhong, Z. Wang, J. Chen, *Adv. Mater.* **2021**, *33*, 2101316.

[39] A. K. Jaiswal, D. Wang, V. Wollersen, R. Schneider, M. L. Tacon, D. Fuchs, *Adv. Mater.* **2022**, *34*, 2109163.

[40] Z. Cui, A. J. Grutter, H. Zhou, H. Cao, Y. Dong, D. A. Gilbert, J. Wang, Y.-S. Liu, J. Ma, Z. Hu, J. Guo, J. Xia, B. J. Kirby, P. Shafer, E. Arenholz, H. Chen, X. Zhai, Y. Lu, *Sci. Adv.* **2020**, *6*, eaay0114.

[41] R. Ramos, S. K. Arora, I. V. Shvets, *Phys. Rev. B* **2008**, *78*, 214402.

[42] A. Annadi, Z. Huang, K. Gopinadhan, X. R. Wang, A. Srivastava, Z. Q. Liu, H. H. Ma, T. P. Sarkar, T. Venkatesan, Ariando, *Phys. Rev. B* **2013**, *87*, 201102(R).

[43] T. Li, L. Zhang, X. Hong, *J Vac Sci Technol A* **2022**, *40*, 010807.

[44] Y. Miao, X. Chen, S. Yang, K. Zheng, Z. Lian, Y. Wang, P. Wang, C. Gao, D.-Z. Yang, D.-S. Xue, *J. Magn. Magn. Mater.* **2020**, *512*, 167013.

[45] Y. Miao, D. Yang, L. Jia, X. Li, S. Yang, C. Gao, D. Xue, *Appl. Phys. Lett.* **2021**, *118*, 042404.